engineering proceedings

MDPI

Article

Active Reconfigurable Intelligent Surface (ARIS)-Empowered Satellite Positioning Approach for Indoor Environments †

Yu Zhang [1], Xin Sun [1], Tianwei Hou [1,2,*], Anna Li [3], Sofie Pollin [4], Yuanwei Liu [5] and Arumugam Nallanathan [2,6]

[1] School of Electronic and Information Engineering, Beijing Jiaotong University, Beijing 100044, China; 25110072@bjtu.edu.cn (Y.Z.); xsun@bjtu.edu.cn (X.S.)
[2] School of Electronic Engineering and Computer Science, Queen Mary University of London, London E1 4NS, UK; a.nallanathan@qmul.ac.uk
[3] School of Computing and Communications, Lancaster University, Lancaster LA1 4WA, UK; a.li16@lancaster.ac.uk
[4] Department of Electrical Engineering (ESAT), KU Leuven, 3001 Leuven, Belgium; sofie.pollin@esat.kuleuven.be
[5] Department of Electrical and Electronic Engineering, The University of Hong Kong, Hong Kong; yuanwei@hku.hk
[6] Department of Electronic Engineering, Kyung Hee University, Yongin-si 17104, Gyeonggi-do, Republic of Korea
* Correspondence: twhou@bjtu.edu.cn
† Presented at the European Navigation Conference 2025 (ENC 2025), Wrocław, Poland, 21–23 May 2025.

Abstract

To mitigate the loss of satellite navigation signals in indoor environments, we propose an active reconfigurable intelligent surface (ARIS)-empowered satellite positioning approach. Deployed on building structures, ARIS reflects navigation signals to indoor receivers to bypass obstructions, providing high-precision positioning services to receivers in non-line-of-sight (NLoS) areas. The path between ARIS and the receiver is defined as the extended line-of-sight (ELoS) path, and an improved carrier phase observation equation is derived to accommodate this path. The receiver compensates for its clock bias through network time synchronization, corrects the actual satellite–ARIS–receiver signal path to the satellite–receiver distance through a distance correction algorithm, and determines the position using the least squares (LS) method. Simulation results show that the proposed method provides positioning services with errors not exceeding 4 m in indoor environments, with time synchronization accuracy within an error range of 10 ns.

Keywords: global navigation satellite system (GNSS); indoor environments; reconfigurable intelligent surface (RIS)

1. Introduction

The global navigation satellite system (GNSS) is widely acknowledged for its provision of high-precision all-weather positioning and timing services [1] which are extensively applied across various global applications, especially in critical industries such as transportation, telecommunications, and agriculture [2]. Traditional GNSS relies on the line-of-sight (LoS) signals for precise positioning [3]. Under unobstructed signal conditions, the receiver can achieve positioning by using navigation signals from at least four satellites. However, in indoor environments the LoS signals from satellites are often blocked by buildings, which makes it difficult for GNSS receivers to acquire sufficient satellite signals [4]. As urbanization continues, high-accuracy positioning challenges in indoor environments have become increasingly prominent [5].

Academic Editor: Tomasz Hadaś

Published: 7 April 2026

To address these issues, we turn our focus to the reconfigurable intelligent surface (RIS), an emerging communication technology. RIS is a kind of planar material that can be deployed on the exterior surfaces of buildings; its working principle is similar to mirror reflection [6,7]. When electromagnetic signals reach the RIS, it can automatically adjust its electromagnetic parameters, transforming the transmission path into a controllable form by reflecting the signals. Considering the low power intensity of satellite navigation signals, traditional RIS may face challenges in providing reliable positioning support under these conditions. To address these limitations, we introduce active RIS (ARIS) to the GNSS context. Compared to RIS, ARIS can actively amplify navigation signals at the cost of some power consumption thanks to its integration of amplifier components [8,9]. Additionally, the positioning errors introduced by the ARIS array from phase shifts, beamwidth, and hardware delays are all predictable and manageable, making it a reliable solution for accurate positioning.

In this work, we propose an ARIS-empowered satellite positioning network. When LoS signals are completely blocked, the reflection characteristics of ARIS can be utilized to create an extended LoS (ELoS) path, which refers to the path between the ARIS and the receiver.

However, the proposed ARIS-empowered satellite positioning approach poses three challenges: (i) due to the existence of the ELoS path, traditional carrier-phase observation is no longer applicable to the proposed scenario; (ii) the ELoS path is shared by multiple satellites, which if not properly accounted for can result in a shifted position estimate; and (iii) the receiver clock bias and ELoS path propagation time are coupled, as both influence the signal's travel time, making it challenging to separate their effects on positioning. To address these challenges, we introduce a new carrier phase observation equation to accommodate the novel navigation signal transmission path. Network time synchronization technology is employed to decouple the transmission time of the ELoS path from the receiver clock bias instead of relying on traditional GNSS algorithms to calculate the clock bias. Additionally, a geometric correction method is applied to rectify the ranging errors caused by the ELoS path. With the development of 5G, the precision requirements for time synchronization have increased. China Mobile's research has achieved ultra-high-precision synchronization reaching 5 ns, which provides the technical feasibility for the implementation of our work [10].

We validated the proposed approach in simulated indoor environments. The experimental results show that when the ARIS can detect more than five satellites and the network time synchronization error is controlled within ±10 ns, the positioning error for indoor receivers is within 4 m.

2. System Model

2.1. Channel Model and Signal Propagation Model

Wireless signals are essentially electromagnetic waves propagating in 3D space. For ARIS, Love's field equivalence principle states that the electromagnetic field inside and outside a closely packed surface can be uniquely determined by the currents and magnetic fields on the surface. Assuming that the ARIS array has K elements, the intensity and distribution of these equivalent currents within each element are determined by the incident signals $\psi(t)$. The reflected signals $\psi_k(t)$ at the k-th element can be represented as follows:

$$\psi_k(t) = R_k \psi(t) \tag{1}$$

https://doi.org/10.3390/engproc2026126045

where R_k represents the reflection complex coefficient of the k-th element. According to the law of energy conservation, for an ARIS element, the following constraints on the local reflection coefficients must be satisfied:

$$|R_k|^2 \leqslant H_{amp} \tag{2}$$

where H_{amp} is the amplification factor.

For convenience of designing ARIS in wireless communication systems, these narrowband frequency-flat coefficients are rewritten in terms of their amplitude and phase shift as follows:

$$R_k = \sqrt{\beta_k} e^{j\theta_k} \tag{3}$$

where β_k are real-valued coefficients satisfying $\beta_k \leqslant H_{amp}$ and θ_k are the phase shifts introduced by the k-th element for the reflected signals.

The channel vector $\boldsymbol{h}^i$ between the i-th satellite and the ARIS elements is expressed as

$$\boldsymbol{h}^i = \begin{bmatrix} h_1^i & h_2^i & \cdots & h_k^i & \cdots & h_K^i \end{bmatrix}^T, \tag{4}$$

where h_k^i represents the channel response between the i-th satellite and the k-th ARIS element, with $|h_k^i|$ following a Rician distribution.

The reflected channel matrix $\boldsymbol{g}$ between the ARIS and the receiver in indoor environments is

$$\boldsymbol{g} = \begin{bmatrix} g_1 & g_2 & \cdots & g_k & \cdots & g_K \end{bmatrix}^T, \tag{5}$$

where g_k represents the reflected channel response between the k-th ARIS element and the receiver.

Therefore, the signal $\zeta^i(t)$ from the i-th satellite via ARIS is expressed as

$$\zeta^i(t) = \left(\boldsymbol{g}^T \boldsymbol{R} \boldsymbol{h}^i r_{i,Rs}^{-\frac{\alpha_1}{2}} r_{Ru}^{-\frac{\alpha_2}{2}} \right) \sqrt{P} \psi(t) + N_0, \tag{6}$$

where $\boldsymbol{R}$ denotes the diagonal matrix with $\boldsymbol{R} = diag[\ \beta_1 e^{j\theta_1} \quad \beta_2 e^{j\theta_2} \quad \cdots \quad \beta_k e^{j\theta_k}\ ]$, $r_{i,Rs}$ and r_{Ru} represent the distance between the i-th satellite and the ARIS and the distance between the ARIS and the receiver, respectively, α_1 and α_2 denote the path loss exponent of the satellite-ARIS link and the ARIS-receiver link (with $r_{i,Rs}^{-\frac{\alpha_1}{2}}$ and $r_{Ru}^{-\frac{\alpha_2}{2}}$ representing the large-scale fading components of the signal), P denotes the transmit power of the navigation signal, and N_0 denotes the additive white Gaussian noise (AWGN).

Additionally, when navigation signals reach the ARIS, phase differences occur at each ARIS element due to the varying distances between the signal source and the elements. The ARIS analyzes these phase differences to estimate the signal's angle of arrival (AoA). Simultaneously, by controlling the phase and amplitude of each element, the ARIS introduces specific phase shifts to the transmitted signals, thereby calculating the angle of departure (AoD) to achieve directional transmission.

2.2. Positioning Model

According to [11], the direct carrier phase observation $\tilde{\varphi}_i$ between the i-th navigation satellite and the receiver at the observation epoch can be described by

$$\tilde{\varphi}_i \lambda = r_{i,su} - cT_u + cT^i - N_i \lambda - V_{i,ion} - V_{i,trop} + \varepsilon, \tag{7}$$

where $\tilde{\varphi}_i$ denotes the carrier phase observation obtained by the receiver, λ is the wavelength of the satellite signals, $r_{i,su}$ represents the geometric distance between the receiver and the

i-th satellite, c is the speed of light in vacuum, T_u is the receiver clock bias, T^i is the satellite clock bias, N_i is the integer ambiguity, $V_{i,ion}$ and $V_{i,trop}$ are the ionospheric and tropospheric delays, respectively, and ε represents the unmodeled errors, including measurement noise and multipath effects.

By compensating for the modeled errors and delays and ignoring the unmodeled errors, the carrier phase observation equation can be simplified to

$$\varphi_i \lambda = r_{i,su} - cT_u + \varepsilon. \tag{8}$$

According to Figure 1, in the proposed ARIS empowered satellite positioning network, the propagation distance changes from $r_{i,su}$ to $r_{i,Rs} + r_{Ru} + \omega$, where ω denotes the distance error introduced by ARIS. Based on the physical model of signal propagation aided by ARIS, Equation (8) can be rewritten as

$$\varphi_i \lambda = r_{i,Rs} + r_{Ru} - cT_u + \varepsilon + \omega. \tag{9}$$

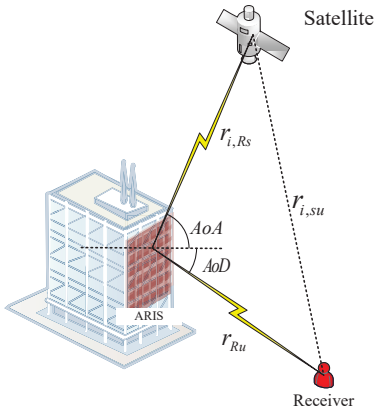

Figure 1. Illustration of ARIS reflection channel.

The distance between the ARIS and receiver can be expressed as follows:

$$r_{Ru} = cT_R \tag{10}$$

where T_R is the time of flight from ARIS to the receiver.

Based on Equation (10), combining the receiver clock bias and the propagation time of the signal from ARIS to the receiver, Equation (9) can be rewritten as

$$\varphi_i \lambda = r_{i,Rs} - c(T_u - T_R) + \varepsilon + \omega. \tag{11}$$

Based on Equation (11), it is important to note that the presence of multiple phase measurements φ_i allows us to estimate the position of the ARIS. However, the two parameters T_u and T_R are jointly estimated in all calculations. Therefore, these two parameters cannot be independently separated during the analytical process. To address this issue, we introduce network time synchronization in Section 3 to effectively disentangle the effects of T_u and T_R, thereby improving positioning accuracy and the reliability of signal processing.

3. ARIS-Empowered Positioning Approach

3.1. ARIS Position Calculation Algorithm

By observing signals from i satellites, we can derive the following carrier phase observation equations:

$$\begin{cases} \varphi_1\lambda = r_{1,Rs} - c(T_u - T_R) + \varepsilon + \omega \\ \varphi_2\lambda = r_{2,Rs} - c(T_u - T_R) + \varepsilon + \omega \\ \cdots \\ \varphi_i\lambda = r_{i,Rs} - c(T_u - T_R) + \varepsilon + \omega \end{cases} \tag{12}$$

where $r_{i,Rs} = \sqrt{(x^i - x_R)^2 + (y^i - y_R)^2 + (z^i - z_R)^2}$. The coordinates (x^i, y^i, z^i) can be obtained by the receiver through the ephemeris broadcast by the satellite. Expanding the position (x_0, y_0, z_0) around (x_R, y_R, z_R) using a Taylor series, the linearized measurement equation is obtained as follows:

$$\Delta r_i \approx \frac{x^i - x_0}{r^i}\Delta x + \frac{y^i - y_0}{r^i}\Delta y + \frac{z^i - z_0}{r^i}\Delta z + c\Delta T \tag{13}$$

where $\Delta r_i = \varphi_i\lambda - r^i$ represents the residual between the carrier phase observation received by the receiver and the calculated value at the Taylor expansion point, r^i is the geometric distance between the i-th satellite and the expansion point, $\Delta x = x_R - x_0$, $\Delta y = y_R - y_0$, $\Delta z = z_R - z_0$, and $T = T_u - T_R$. For simplicity, Equation (13) can be rewritten in compact form as

$$\Delta\mathbf{r} = \mathbf{A} \times \mathbf{B}, \tag{14}$$

where

$$\Delta\mathbf{r} = \begin{bmatrix} \Delta r_1 \\ \Delta r_2 \\ \vdots \\ \Delta r_i \end{bmatrix}, \quad \mathbf{B} = \begin{bmatrix} \Delta x \\ \Delta y \\ \Delta z \\ \Delta T \end{bmatrix}, \mathbf{A} = \begin{bmatrix} \frac{x^1 - x_0}{r^1} & \frac{y^1 - y_0}{r^1} & \frac{z^1 - z_0}{r^1} & c \\ \frac{x^2 - x_0}{r^2} & \frac{y^2 - y_0}{r^2} & \frac{z^2 - z_0}{r^2} & c \\ \vdots & \vdots & \vdots & \vdots \\ \frac{x^i - x_0}{r^i} & \frac{y^i - y_0}{r^i} & \frac{z^i - z_0}{r^i} & c \end{bmatrix} \tag{15}$$

Clearly, there are four unknown parameters in Equation (15). When the receiver can detect signals transmitted from at least four satellites, the equation is solvable. Thus, the ordinary LS solution to Equation (14) is given by

$$\hat{\mathbf{B}} = \left(\mathbf{A}^T\mathbf{A}\right)^{-1}\mathbf{A}^T\Delta\mathbf{r}. \tag{16}$$

The n-th iteration solution is

$$\begin{bmatrix} x_n & y_n & z_n & T_n \end{bmatrix}^T = \begin{bmatrix} x_{n-1} & y_{n-1} & z_{n-1} & T_{n-1} \end{bmatrix}^T + \begin{bmatrix} \Delta x & \Delta y & \Delta z & \Delta T \end{bmatrix}^T. \tag{17}$$

Following Equation (16), the variation vector $\hat{\mathbf{B}}$ is determined and added to the initial estimate to obtain an updated iterative value. The process is repeated until the norm $\|\hat{\mathbf{B}}\|$ falls below a predefined threshold, at which point the vector $[x_n, y_n, z_n]$ represents the 3D coordinates of the ARIS.

3.2. ELoS Path Distance Estimation

In this subsection, we use network time synchronization to calculate the distance of the ELoS path. The receiver accesses mobile networks, enabling ultra-high precision synchronization with the clock from the timing service center. With the receiver clock

bias controlled within the timing accuracy range, the timing offset in iteration n (T_n in Equation (17)) can be approximated as

$$T_n \approx -\hat{T}_R + \gamma, \tag{18}$$

where $\hat{T}_R$ denotes the computed signal transmission time of the ELoS path and γ represents the network time synchronization error. Therefore, the ELoS path distance is calculated as

$$r_{Ru} = c\,\hat{T}_R. \tag{19}$$

3.3. Distance Correction and Receiver Positioning Algorithm

After obtaining the position of ARIS and the ELoS path distance, this subsection uses the acquired information along with the AoA and AoD provided by ARIS to implement satellite–receiver path correction and achieve receiver positioning.

ARIS is capable of calculating the AoA θ_{AoA} and AoD θ_{AoD}, as shown in Figure 1. When reflecting signals, ARIS broadcasts the angle information to the receiver simultaneously. Thus, the receiver can calculate the geometric angle α_i of the ELoS path and the corresponding cosine value χ_i, as follows:

$$\alpha_i = (\theta_{AoA})_i + \theta_{AoD}. \tag{20}$$

$$\chi_i = \cos\alpha_i. \tag{21}$$

As shown in Figure 1, the geometric distance between the satellite and the receiver can be calculated by solving the triangle formed by the satellite, ARIS, and the receiver. Combining Equation (21) and using the cosine rule of the triangle, the distance between the satellite and the receiver is obtained as

$$\tilde{r}_{i,su} = \sqrt{(r_{i,Rs})^2 + r_{Ru}^2 - 2r_{i,Rs}r_{Ru}\chi_i}. \tag{22}$$

The distance between the satellite and the receiver in Equation (22) can also be expressed in coordinate form as

$$r_{i,su} = \sqrt{(x^i - x_u)^2 + (y^i - y_u)^2 + (z^i - z_u)^2}. \tag{23}$$

By synthesizing the receiver's continuous reception of signals from multiple satellites, the following geometric distance equations are obtained:

$$\begin{cases} \tilde{r}_{1,su} = r_{1,su} + \rho_1 \\ \tilde{r}_{2,su} = r_{2,su} + \rho_2 \\ \qquad\vdots \\ \tilde{r}_{i,su} = r_{i,su} + \rho_i \end{cases} \tag{24}$$

where ρ_i represents the calculation error, primarily caused by quantization errors and AoA/AoD angle estimation errors.

Using Taylor series expansion for Equation (23) as in Equation (13)–(16) and employing the 3D coordinates of ARIS obtained from Equation (17) as initial values, the LS algorithm is used iteratively until the positioning results converge to a predefined threshold, at which point the 3D coordinates of the receiver are determined.

https://doi.org/10.3390/engproc2026126045

4. Results

In this section, we present the simulation results of the ARIS-empowered satellite positioning approach in indoor environments. In the simulation, (−2,604,298.533, 4,743,297.217, 3,364,978.513) served as the initial position of the receiver in indoor environments, with the ARIS (−2,604,348.533, 4,743,312.217, 3,364,998.513) deployed on a building at an elevation of 40 m above ground level. The ARIS could receive navigation signals transmitted by at least 12 satellites, while the receiver was unable to receive any LoS signals from the satellites.

Throughout the simulation, the satellite position, satellite clock bias, integer ambiguity, ionospheric delay, and tropospheric delay were obtained in advance through model calculations. The receiver was connected to network time synchronization for clock correction.

4.1. Positioning Results of the ARIS

In the positioning process, the number of satellites observed by the receiver via the ELoS path is typically not constant. Therefore, it is crucial to study the positioning accuracy under different satellite quantities. To this end, we tested the positioning results with 4 to 12 satellites during the positioning of the ARIS at the receiver, comparing the accuracy under varying satellite counts.

We chose six observable satellites and conducted another 1000 Monte Carlo simulations. The corresponding 3D coordinate errors are shown in Figure 2. The distribution of errors along the X, Y, and Z axes shows that most positioning errors on the X and Y axes are within 1.5 m, while Z-axis errors are within 2.5 m.

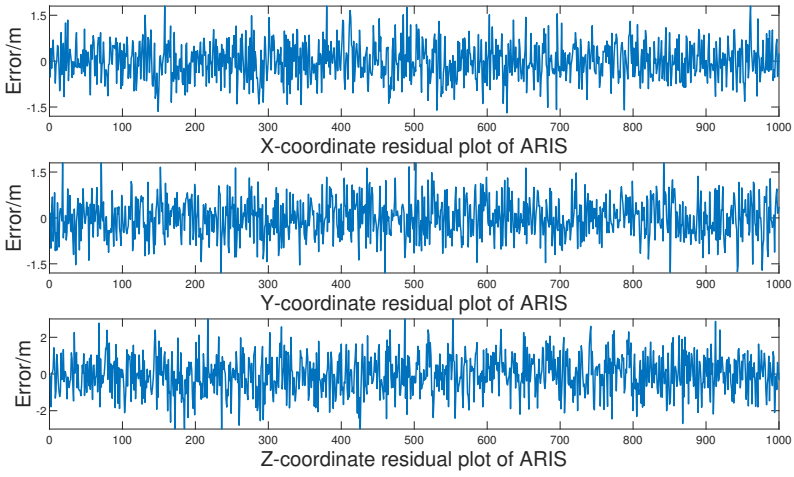

Figure 2. 3D positioning error plot of ARIS with six satellites.

To further analyze the impact of different satellite counts on positioning accuracy, we calculated the root mean square error (RMSE) for each case. As shown in Figure 3, when five satellites are observable, the RMSE is around 1.6 m with fluctuations. When the satellite count increases to six, the RMSE decreases to 1.2 m with reduced fluctuation. As the number of satellites further increases, the positioning performance continues to improve; with eight satellites the RMSE drops to 0.8 m, and with twelve it further decreases to 0.5 m with minimal fluctuation. The results show that when the number of observable satellites reaches five or more, the positioning performance of ARIS significantly improves with decimeter-level accuracy achieved when the number exceeds eight.

https://doi.org/10.3390/engproc2026126045

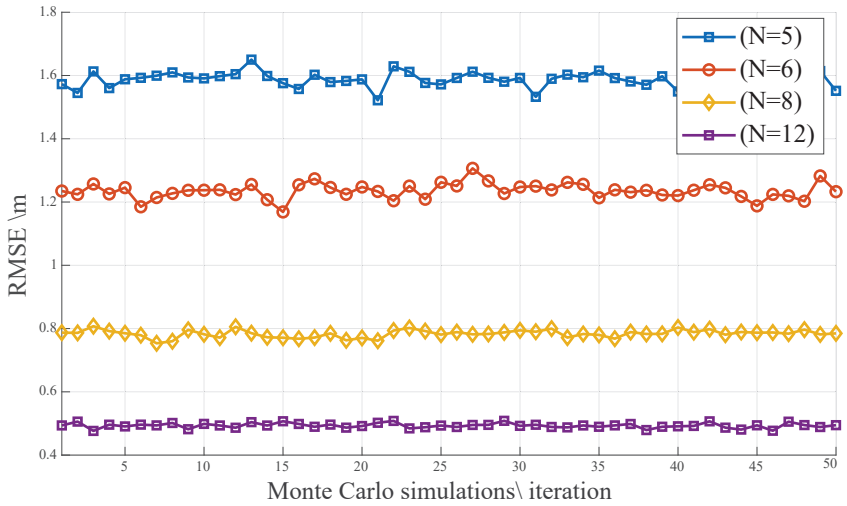

Figure 3. RMSE with different numbers of satellites in ARIS positioning.

4.2. Positioning Results of the Receiver

We also investigated the positioning accuracy of the receiver empowered by ARIS under different network time synchronization errors and satellite counts.

Figure 4 illustrates the receiver positioning errors under different network time synchronization precisions in indoor environments, ranging from 1 ns to 10 ns. When five satellites are observable, the positioning error corresponding to a timing error of 10 ns is 5.6 m. The error decreases as the network time synchronization error is reduced. With six observable satellites, the positioning error for a 10 ns timing error reduces to 3.9 m. With eight satellites, the error lies between 1 and 4 m, and with twelve satellites the error further decreases to a range of 0 to 3 m, with minimal fluctuation. The difference between the cases with eight and twelve satellites is approximately 0.4 m. These results indicate that due to the influence of beamwidth and ARIS positioning errors, increasing the satellite count beyond eight only slightly improves positioning accuracy.

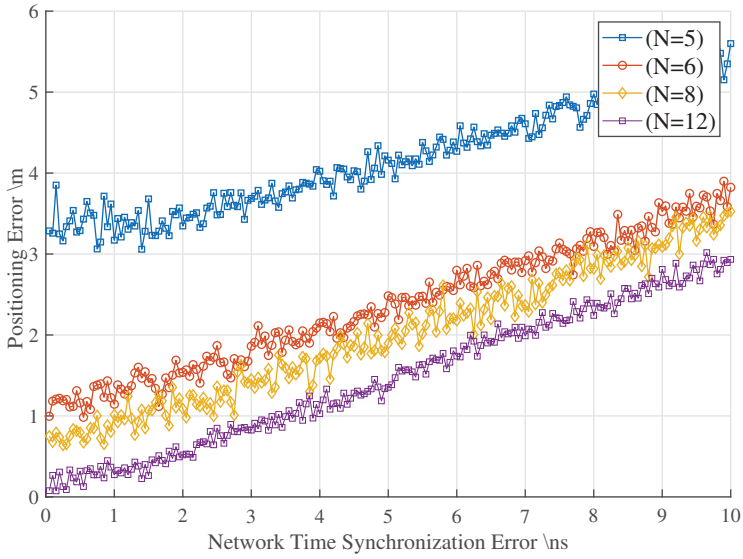

Figure 4. Receiver positioning errors under different timing accuracies with N satellites in indoor environments.

https://doi.org/10.3390/engproc2026126045

5. Conclusions

We introduce an ARIS empowered satellite positioning approach, offering a new positioning solution for receivers in indoor environments. We first review the challenges faced by existing positioning techniques, then discuss the features and benefits of ARIS. Based on traditional positioning models, we develop an ELoS path empowered by ARIS and derive a corresponding carrier-phase observation model. Next, we design an ARIS-empowered satellite positioning approach, including the ARIS position calculation algorithm, ELoS path distance estimation, satellite-to-receiver distance correction algorithm, and receiver positioning algorithm. An important future direction is to extend the proposed ARIS-empowered satellite positioning approach to low-Earth orbit (LEO) satellites by addressing issues such as high speeds and limited coverage areas.

Author Contributions: Conceptualization: Y.Z. and T.H.; methodology and validation: Y.Z., X.S., A.L., and Y.L.; formal analysis: T.H., X.S., and A.N.; investigation: Y.Z. and A.L.; writing—original draft preparation: Y.Z.; writing—review and editing: X.S., T.H., S.P., and A.N.; visualization: T.H. and S.P.; project administration: S.P. and A.N. All authors have read and agreed to the published version of the manuscript.

Funding: This work was supported in part by the Fundamental Research Funds for the Central Universities under Grants 2023JBZY012 and 2024JBMC014, in part by the National Natural Science Foundation for Young Scientists of China under Grant 62201028, in part by the Young Elite Scientists Sponsorship Program by CAST under Grant 2022QNRC001, in part by the Beijing Natural Science Foundation L232041, and in part by the Marie Skłodowska-Curie Fellowship under Grant 101154499, as well as by EPSRC under EP/W004100/1, EP/W034786/1, and EP/Y037243/1.

Institutional Review Board Statement: Not applicable.

Informed Consent Statement: Not applicable.

Data Availability Statement: The data presented in this study are available on request from the corresponding author.

Conflicts of Interest: The authors declare no conflicts of interest.

References

1. Zhu, N.; Marais, J.; Bétaille, D.; Berbineau, M. GNSS Position Integrity in Urban Environments: A Review of Literature. *IEEE Trans. Intell. Transp. Syst.* **2018**, *19*, 2762–2778. [CrossRef]
2. Wickert, J.; Cardellach, E.; Martín-Neira, M.; Bandeiras, J.; Bertinoaz, et al. GEROS-ISS: GNSS REflectometry, Radio Occultation, and Scatterometry Onboard the International Space Station. *IEEE J. Sel. Top. Appl. Earth Obs. Remote Sens.* **2016**, *9*, 4552–4581. [CrossRef]
3. Zidan, J.; Adegoke, E.I.; Kampert, E.; Birrell, S.A.; Ford, C.R.; Higgins, M.D. GNSS Vulnerabilities and Existing Solutions: A Review of the Literature. *IEEE Access* **2021**, *9*, 153960–153976. [CrossRef]
4. More, H.; Cianca, E.; De Sanctis, M. Positioning Performance of LEO Mega Constellations in Deep Urban Canyon Environments. In *Proceedings of the 25th International Symposium on Wireless Personal Multimedia Communications (WPMC)*; IEEE: Piscataway, NJ, USA, 2022; pp. 256–260.
5. Yuan, Y.; Shen, F.; Li, X. GPS Multipath and NLOS Mitigation for Relative Positioning in Urban Environments. *Aerosp. Sci. Technol.* **2020**, *107*, 106315. [CrossRef]
6. Liu, Y.; Liu, X.; Mu, X.; Hou, T.; Xu, J.; Di Renzo, M.; Al-Dhahir, N. Reconfigurable Intelligent Surfaces: Principles and Opportunities. *IEEE Commun. Surv. Tutorials* **2021**, *23*, 1546–1577. [CrossRef]
7. Xu, J.; Liu, Y.; Mu, X.; Dobre, O.A. STAR-RISs: Simultaneous Transmitting and Reflecting Reconfigurable Intelligent Surfaces. *IEEE Commun. Lett.* **2021**, *25*, 3134–3138. [CrossRef]
8. Zhang, Z.; Dai, L.; Chen, X.; Liu, C.; Yang, F.; Schober, R.; Poor, H.V. Active RIS vs. Passive RIS: Which Will Prevail in 6G? *IEEE Trans. Commun.* **2023**, *71*, 1707–1725. [CrossRef]
9. Zhi, K.; Pan, C.; Ren, H.; Chai, K.K.; Elkashlan, M. Active RIS Versus Passive RIS: Which is Superior With the Same Power Budget? *IEEE Commun. Lett.* **2022**, *26*, 1150–1154. [CrossRef]

10. Satka, Z.; Ashjaei, M.; Fotouhi, H.; Daneshtalab, M.; Sjödin, M.; Mubeen, S. A comprehensive systematic review of integration of time sensitive networking and 5g communication. *J. Syst. Archit.* **2023**, *138*, 102852. [CrossRef]
11. Saastamoinen, J. Atmospheric correction for the troposphere and stratosphere in radio ranging satellites. *Geophys. Monogr. Ser.* **1972**, *15*, 247–251.